

VLT/SPHERE MULTI-WAVELENGTH HIGH-CONTRAST IMAGING OF THE HD 115600 DEBRIS DISK: NEW CONSTRAINTS ON THE DUST GEOMETRY AND THE PRESENCE OF YOUNG GIANT PLANETS

AIDAN GIBBS,¹ KEVIN WAGNER,^{1,2,3} DANIEL APAI,^{1,3,4} ATTILA MOÓR,⁵ THAYNE CURRIE,^{6,7,8} MICKÄEL BONNEFOY,⁹
MAUD LANGLOIS,^{10,11} AND CAREY LISSE¹²

¹*Steward Observatory, The University of Arizona, 933 N. Cherry Avenue, Tucson, AZ 85721, USA*

²*NSF Graduate Research Fellow*

³*NASA Nexus For Exoplanetary System Science: Earths in Other Solar Systems Team*

⁴*Lunar and Planetary Laboratory, The University of Arizona, 1640 E. University Boulevard, Tucson, AZ 85718, USA*

⁵*Konkoly Observatory, MTA CSFK, Konkoly-Thege Miklós út 15-17, H-1121 Budapest, Hungary*

⁶*Subaru Telescope, National Astronomical Observatory of Japan, 650 North A'ohökü Place, Hilo, HI 96720, USA*

⁷*NASA-Ames Research Center, Moffett Field, CA, USA*

⁸*Eureka Scientific, 2452 Delmer Street Suite 100, Oakland, CA, USA*

⁹*Max Planck Institute for Astronomy*

¹⁰*Centre de Recherche Astrophysique de Lyon (CRAL)*

¹¹*Aix Marseille Université, CNRS, LAM (Laboratoire d'Astrophysique de Marseille)*

¹²*Johns Hopkins University Applied Physics Laboratory*

ABSTRACT

Young and dynamically active planetary systems can form disks of debris that are easier to image than the planets themselves. The morphology and evolution of these disks can help to infer the properties of the putative planets responsible for generating and shaping the debris structures. We present integral field spectroscopy and dual-band imaging from VLT/SPHERE (1.0–1.7 μ m) of the debris disk around the young F2V/F3V star HD 115600. We aim to 1) characterize the geometry and composition of the debris ring, 2) search for thermal emission of young giant planets, and 3) in the absence of detected planets, to refine the inferred properties of plausible planets around HD 115600 to prepare future attempts to detect them. Using a different dust scattering model (ZODIPIC) than in the discovery paper (Henyey-Greenstein) to model the disk geometry, we find $a_0 = 46 \pm 2$ au for the disk's central radius and offsets $\Delta\alpha, \Delta\delta = -1.0 \pm 0.5, 0.5 \pm 0.5$ au. This offset is smaller than previously found, suggesting that unseen planets of lower masses could be sculpting the disk. Spectroscopy of the disk in Y-J bands with SPHERE shows reddish color, which becomes neutral or slightly blue in H band seen with GPI, broadly consistent with a mixed bulk disk composition of processed organics and water ice. While our observed field contains numerous background objects at wide separations, no exoplanet has been directly observed to a mass sensitivity limit of 2–3(5–7) M_J between a projected separation of 40 and 200 au for hot (cold)-start models.

1. INTRODUCTION

Debris disks provide important clues to the late stages of planet formation (e.g., Jang-Condell et al. 2015; Apai et al. 2015). Second-generation dust disks can be produced by young, active planetary systems in which collisional cascades generate large amounts of dust, observable in infrared and longer wavelengths (Wyatt 2008; Gáspár et al. 2012). Surveys have also shown that giant planets are more frequently found at large separations around stars with debris disks (Meshkat et al. 2017). Planets can interact with the disk to produce large-scale structures (rings, warps, spirals, etc.) that are often easier to observe than the planets themselves (e.g., Su et al. 2013; Matthews et al. 2017; Currie et al. 2017). Thus, stars with debris disks are not only good places to look for exoplanets, but disk structures can also be used to predict and constrain unseen planets for possible future detections and studies.

The Scorpius-Centaurus OB association is an optimal target for disk studies, due to its proximity (~ 100 -200 pc) and large collection of young systems. A high fraction of early-type Sco-Cen stars show strong infrared excess indicative of copious circumstellar dust (Carpenter et al. 2009; Chen 2014; Jang-Condell et al. 2015; Pecaute & Mamajek 2016). Sco-Cen includes many of the currently known directly-imaged planetary companions (e.g. Rameau et al. 2013; Quanz et al. 2013; Bailey et al. 2014; Currie et al. 2015a; Chauvin et al. 2017; Keppler et al. 2018) and numerous debris disks resolved in scattered light (e.g. Thalmann et al. 2013; Currie et al. 2015b; Lagrange et al. 2016; Matthews et al. 2017; Bonnefoy et al. 2017).

HD 115600 (HIP 64995) is an F2V/F3V star located in the Lower Centaurus Crux region of the Sco-Cen OB Association whose debris disk could provide key insights into the planet formation. It has a measured distance of 109.6 ± 0.5 pc (Gaia Collaboration et al. 2018) and is estimated to be ~ 15 Myr old (Pecaute et al. 2012; Pecaute & Mamajek 2016). The system was first observed to have an infrared excess by Spitzer/MIPS, with a fractional luminosity $L_{IR}/L_* = 1.7 \times 10^{-3}$ and dust mass $0.03 M_{moon}$ (Chen et al. 2011), consistent with an extremely luminous dusty debris disk. Using the Gemini Planet Imager, Currie et al. (2015b) obtained the first images of the HD 115600 debris disk, resolving it into a bright ring-like structure. Given the system's age, the primary's mass and birth environment, and the disk's stellocentric distance, they hypothesized that the disk may be a good analogue for the early Kuiper belt. Its H-band spectrum is at least broadly consistent with predictions for a water ice composition, although other compositions could not be ruled out. By fitting an ellipse to the debris ring, they inferred a semi-major axis of 48 ± 1.1 au, an eccentricity of 0.1-0.2, and a disk offset of $\Delta\alpha, \Delta\delta = 0''.018 \pm 0''.008, 0''.029 \pm 0''.014$ ($2.0 \pm 0.9, 3.2 \pm 1.5$ au from the central star). To explore ad-

ditional disk properties, Currie et al. (2015b) created scattered light disk models using a Henyey-Greenstein phase function and forward-modeled them through their reduction pipeline, finding neutral scattering was the best fit. Furthermore, they found that the debris disk is very thick, with a width-to-mean radius ratio of $\Delta r/r_0 \sim 0.37$.

The sharp ring-like structure of the disk may suggest sculpting by a planet (or planets) and the measured offset of the disk further implies that this planet could be massive. Numerical modeling by Thilliez & Maddison (2017) determined that disk structures driven by a $\sim 8M_J$ planet located at ~ 30 au are the best fit to observed morphology. While the predicted contrast (4×10^{-5} in H band) of this hypothetical planet is within the theoretical performance capabilities of current extreme adaptive optics (hereafter extreme AO) instruments such as SPHERE and GPI (Mesa et al. 2015; Bailey et al. 2016), the orientation of the disk ($i = 79^\circ$) makes the detection very challenging.

By analyzing new multi-wavelength extreme AO observations of HD 115600's debris disk with updated models, we can better constrain the disk's geometry, provide new constraints on the system's inventory of massive planets possibly sculpting the disk, and provide new insights into the disk's composition. Numerous debris disk studies including Currie et al. (2015b) interpret scattered light images using the standard, simple Henyey-Greenstein (H-G) scattering phase function. In addition to noting that H-G functions are ad hoc, recent results further challenge their accuracy (Milli et al. 2017; Hughes et al. 2018; Goebel et al. 2018). Empirically derived scattering functions of debris disks more closely resemble a combination of Henyey-Greenstein functions, similar to the phase function of zodiacal light (Graham et al. 2007; Ahmic et al. 2009). Disk modeling with these functions, rather than H-G, may lead to a revision in disk properties. Additionally, spectroscopy covering a wider wavelength range may clarify whether HD 115600's disk composition shows evidence for a single constituent or has mixed dust composition.

In this study, we present new, multi-wavelength images and spectra of the debris disk around HD 115600 taken with VLT/SPHERE. The processed data are presented and described in Section 2. These images provide a more detailed look at the disk structure as well as expanded wavelength coverage in the Y- and J-bands, and the results are discussed in Section 3. To better constrain the disk structure, we model the disk as an optically thin scattering ring using a scattering function derived from zodiacal light (Hong 1985), and present our model in Section 4, with a discussion in Section 5. In Section 6, we examine the new YJ spectra in combination with the H-band data from Currie et al. (2015b). Finally, we provide new limits on the mass and orbit of any unseen

exoplanets in Section 7, and conclude with a summary of our findings in Section 8.

2. OBSERVATIONS AND DATA REDUCTION

HD 115600 was observed on 2015 June 04 as part of ESO Program 095.C-0298, using the Spectro-Polarimetric High-contrast Exoplanet Research (VLT-SPHERE: [Beuzit et al. 2008](#)) instrument. The observations were conducted with the IRDIFS mode which allows operation of the infrared dual-band imager and spectrograph (IRDIS: [Dohlen et al. 2008](#); [Vigan et al. 2010](#)) with the H2 and H3 filters (central wavelengths 1.576 ± 0.052 and $1.667 \pm 0.054 \mu\text{m}$ respectively), simultaneously with the integral field spectrograph (IFS: [Claudi et al. 2008](#); [Mesa et al. 2015](#)) in YJ bands ($0.95 - 1.35 \mu\text{m}$) with a spectral resolution of $R \sim 50$. SPHERE IFS has a narrow field-of-view of ~ 1 arcsecond in radius, with a plate scale of 7.46 mas/pixel, roughly 0.8 au per pixel at the distance of HD115600. IRDIS has a wide field-of-view of $11'' \times 12.5''$, with a lower resolution plate scale of 12.25 mas/pixel ([Claudi et al. 2008](#); [Dohlen et al. 2008](#); [Vigan et al. 2010](#)).

During the observations, the SAXO extreme adaptive optics system ([Fusco et al. 2006](#)) corrected for wavefront errors, and the apodized Lyot coronagraph, which has an occulting mask with radius of $0.''0925$, attenuated the stellar light contribution. Before the observations, a short star-centering sequence was obtained by applying a sinusoidal pattern to the deformable mirror ([Langlois et al. 2013](#)). This deformation creates 4 satellite spots in a diagonal cross pattern around the star that can be used to precisely locate the star center behind the coronagraph. Using this method, the uncertainty in the star center is 0.25 pixels in both the x and y directions ([Mesa et al. 2015](#)). Flux calibrations were obtained before the observation by slewing the star off of the coronagraph while inserting a neutral density filter to avoid saturation. SPHERE obtained 64 images for IFS and 64 for IRDIS with exposure times of 64 seconds each, for a total integrated exposure time of 68 minutes for each of the two instruments. The instrument field derotator was switched off for the observations to allow angular differential imaging in post-processing, and the field rotation during the observation sequence was $\sim 27^\circ$. The key parameters of the observation are summarized in Table 1.

The basic reduction steps for IFS data, including dark current subtraction, flat field division, microspectra extraction, and wavelength calibration, were performed using a combination of the ESO SPHERE pipeline (version 0.15.0, [Pavlov et al. 2008](#)) and the custom IDL tools described in [Vigan et al. 2015](#). These tools add some additional pre-processing steps beyond those of the pipeline, such as bad pixel correction using the IDL procedure MASKINTERP, and cross-talk correction (spurious light contamination between integral field

unit lenslets). Small scale cross-talk is corrected using a 41×41 kernel with a Moffatt function to reduce the presence of doubles to the aforementioned satellite spots, which are a result of cross-talk. To reduce the stellar halo and speckle noise which remains after extreme AO coronagraphy, we utilized both angular differential imaging (ADI; [Marois et al. 2006](#)) and spectral differential imaging (SDI; [Racine et al. 1999](#)) techniques. These methods utilize varying field rotation and wavelength respectively to separate astrophysical objects from the speckle noise. We used our own principal component analysis (PCA) based Karhunen Loéve image projection (KLIP; [Soummer et al. 2012](#)) algorithms of ADI and SDI, which are described in [Hanson & Apai \(2015\)](#) and [Apai et al. \(2016\)](#). We used annular PCA, with 15 annuli, 14 pixels in width each, and six angular segments. We retained 7 KL basis vectors for ADI and SDI, with a minimum field rotation of $0.5 \times FWHM$ for ADI, and a minimum speckle radial movement of $1.5 \times FWHM$ for SDI between images. Before the PSF subtraction, we applied a sharpening high-pass filter with a width of 11 pixels to the data to reduce low-frequency noise. The reduced images were stored in x-y- λ (Cartesian and wavelength) cubes, as well as band-averaged flux density images in the Y- and J- bands, which greatly improves signal to noise (S/N) compared to the detection in the individual IFS channels. The first seven frames of the cube were not included in the band-averaged images to eliminate frames impacted by detector persistence from the flux calibration frames. All images for a respective wavelength were combined with a noise-weighted mean ([Bottom et al. 2017](#)). Basic reduction steps for IRDIS data were similarly performed using custom IDL tools for bad pixel correction, dark current subtraction, flat fielding, and star centering. We again used classical and KLIP ADI and SDI techniques for PSF subtraction.

3. RESULTS

We detect the disk in the band-integrated flux density IFS images, shown in Figure 1, with a radial extent from $r \sim 0.''35$ to $0.''48$, corresponding to a projected distance of ~ 39 to 53 au. The disk is also visible in IRDIS images, presented in Figure 2. To estimate the signal-to-noise ratio of the disk, we calculate the noise as the standard deviation of the band-integrated image in circular apertures with widths corresponding to the diffraction limited, full-width half maximum (FWHM, ~ 9 pixels), which do not overlap with the regions where the disk is visible, but are centered at similar radii to disk ansae (~ 55 pixels from image center). The signal is defined as the average pixel value of two circular regions of FWHM radius centered on the north and south disk ansae where signal is highest (center pixels 115x, 190y and 165x, 90y). By this metric, with SPHERE-IFS we achieve a peak SNR ~ 20 in the disk ansae, decreasing in disk regions

Table 1. HD 115600 SPHERE Observations

Date	Instrument	Filter	Total Exposure Time	Sub-Int. Time	#Int.	Average Seeing	Average Airmass
June 4 2015	IFS	YJ (0.96 - 1.34 μm)	~ 68 min	64.0 s	64	1.1"	1.22
June 4 2015	IRDIS	H23 (1.593 - 1.667 μm)	~ 68 min	64.0 s	64	1.1"	1.22

with smaller separations. Currie et al. (2015b) report a peak SNR of ~ 8 in GPI data, where they do not mask the disk or self-subtraction footprints in determining the noise. Using the same approach for calculating noise, the disk’s SNR in the SPHERE data is slightly higher ($\sim 10\%$) than in GPI data.

To look for any additional structure that may be present outside of the disk, we also performed PSF subtractions without high-pass filtering, which can suppress extended and faint features. We did not find evidence for any new disk features. Within a projected distance of ~ 25 au from the star, which is masked in Figures 1 and 2, residual speckle noise dominates the image and we are not able to probe disk structure reliably.

Multi-wavelength coverage is used to discriminate between speckle noise, which scales with wavelength, and point-source detections, which do not. We did not detect any point-sources in the vicinity of the disk within 1" of the star. Point-sources detected in the IRDIS field radially closer than the point labeled 4, shown in Figure 2, exhibit motion visually consistent with background stars due to the proper motion of HD 115600 between GPI and SPHERE image epochs. Multiple epoch data was not attainable for point-sources radially further out than point 4. Appendix A includes the properties for all detected sources in the SPHERE and GPI fields. In Section 7, we will quantify and discuss the contrast and mass-sensitivity limits these observations place on the potential presence of planets in the system based on hot and cold start core-accretion models of planet formation and evolution.

4. DISK MODELS

Our aim with disk modeling is to identify the simplest physically viable model of the disk, accounting for projection and light-scattering effects. By understanding the fundamental geometry, we can later attempt to make predictions about disk sculpting by possible exoplanets. We perform the disk modeling by two independent methods, ellipse fitting and with the model ZODIPIC, in order to assess the accuracy of both. We make no attempt to model the disk at the wavelengths of IRDIS, given the benefits of the IFS data such as extended wavelength coverage compared to previous studies and the smaller inner working angle.

We performed primary modeling of the data using the model ZODIPIC (Kuchner 2012), originally written to

model exozodiacal dust, but which is generally applicable to optically thin debris disks. ZODIPIC is based on the radiative model of zodiacal dust in Kelsall et al. (1998), derived from all-sky data collected by the Cosmic Background Experiment/Diffuse Infrared Background Experiment (COBE/DIRBE). This model was chosen not only for ease-of-use, but because the scattering phase function for zodiacal light (Hong 1985) contained in ZODIPIC resembles those empirically derived from debris disks (Graham et al. 2007; Ahmic et al. 2009). This setup allows us to control the disk size, inclination, offset, and scattering phase function, among other parameters. More complex radiative transfer models could be used, but were not warranted by the data quality and the goals of our study.

The general procedure we used to find a best-fit disk model with ZODIPIC was to produce an evenly spaced grid of disk models with varying geometric parameters, and to subtract them from the raw data to find the model that minimizes the residual disk signal in our processed images without considering noise. The residual was calculated for every model in the grid to avoid local minimums and find the absolute lowest value. ZODIPIC parameters related to the star and instrument performance were kept constant through all models. These include the stellar type, distance ($\sim 109.6 \pm 0.5 pc$), and pixel-scale for SPHERE IFS. ZODIPIC also required the observation wavelength as a parameter, therefore we produced a separate model in each IFS wavelength channel for every geometry. The phase function parameter we used is the standard function included in ZODIPIC from Hong (1985) for wavelengths below 4.2 microns, which covered scattering between 30 and 180 degrees. We do not alter or explore the scattering phase function in the interest of keeping a manageable grid size. The geometric parameters varied within our grid search were position angle, inclination, disk radius, and projected location of the disk’s center. We set the inner and outer disk radius to the approximate visual size, 39 to 53 au, and did not vary these parameters, first to reduce the grid dimensions, and also because we found their variance produced negligible effects in the subtraction residuals. The grid was centered on the best-fit parameters determined by Currie et al. (2015b) using ellipse fitting, which we also performed as a secondary analysis. Table 2 contains our range and step size for the varied parameters.

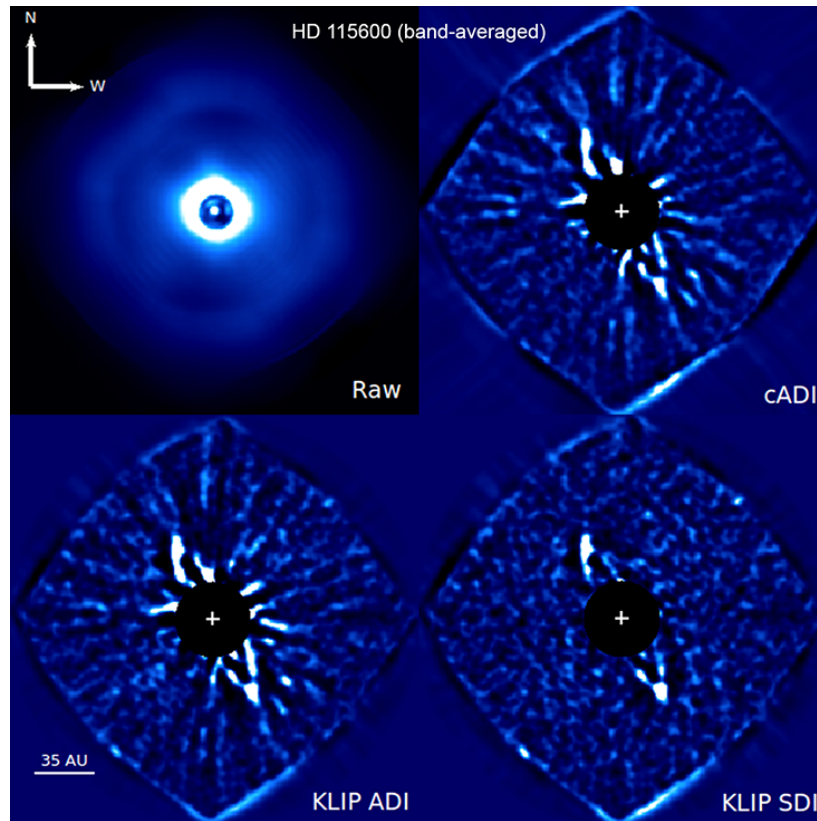


Figure 1. Band-averaged ($0.96 - 1.34 \mu\text{m}$), IFS images of the HD 115600 disk. The raw image is presented in the top left. ADI and SDI reductions are presented in the other 3 panels with high-pass filtering. The disk is clearly visible with ADI and SDI techniques. The image center is marked by a cross in each image, and noise from the central star is masked to ~ 25 au.

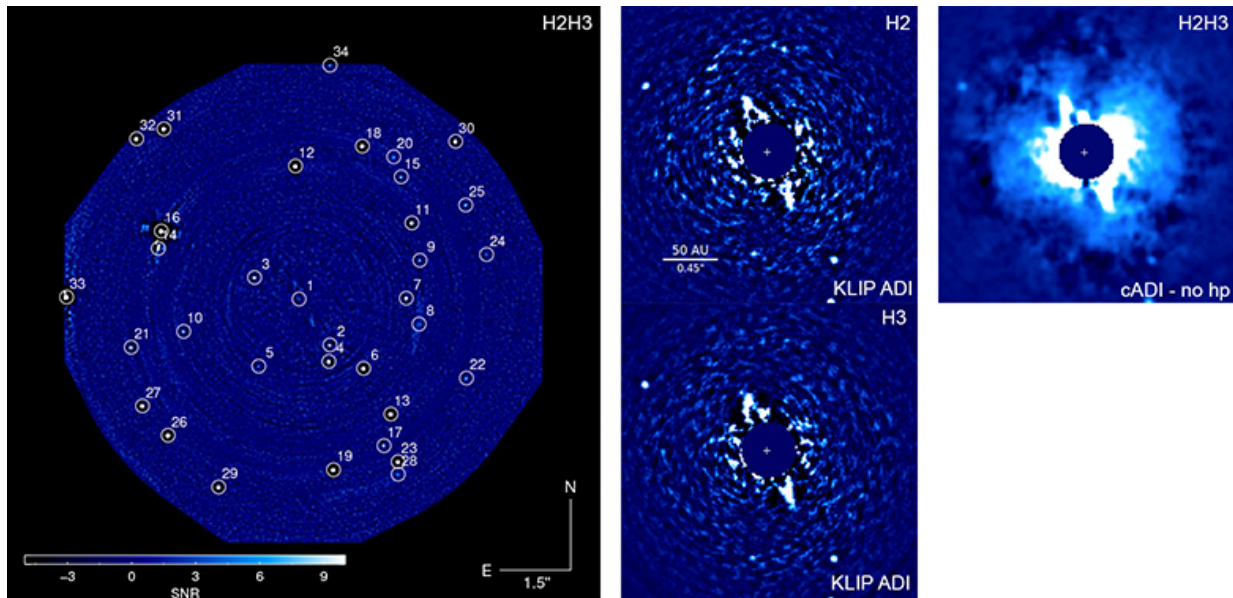


Figure 2. IRDIS dual-band (H23, 1.587 and $1.667 \mu\text{m}$) images of the HD 115600 disk. Left: Signal-to-noise map of the full field-of-view (11 arcseconds) with detected point-sources labeled. The point labeled 1 is a disk feature. Center: KLIP ADI reductions with high-pass filtering for H2 (top) and H3 (bottom) in a region of $2.5''$ around the disk. Right: Classical ADI reduction with no high-pass filtering for the same region in both wavelengths. Noise from the central star is masked in inset images to ~ 25 au with the star center marked by a cross. Note that the brightness scaling changes between left, center, and right.

To subtract a geometric model from our data, we first convolved the model with the measured SPHERE PSF. The width of this PSF was measured from the flux calibration data cube in each wavelength channel. The convolved model was then multiplied by a brightness scale factor, which was initially the same for every wavelength, to bring the brightness of the model to the same approximate brightness as the disk. We subtracted the convolved model from our raw data, and processed it with classical ADI. Classical ADI was chosen to cover a larger parameter space since PCA-based KLIP routines are more computationally expensive. After processing, the disk residuals were measured in the band-averaged images in two circular apertures of 40 pixel (~ 33 au) diameter centered on each disk ansa. These apertures were chosen to avoid strong speckle noise near the image center, but to be large enough to accommodate the range of disk sizes and angles in our grid. The geometry that produced the least-squared residual was adopted as our best-fit. The error is estimated as twice the step size, that is twice the smallest difference between parameter values in our grid, for all grid parameters. The uncertainty in the star centering (0.2 au in x and y) is also considered, but is a minor contribution compared to the step size.

Our final step was to find the optimal brightness of the geometric model in each wavelength channel to further minimize the disk residual after subtraction. We subtracted the geometric model in each channel at varying brightnesses similarly to before, but measured the disk residual in the corresponding channel of the processed data cube instead of the band-averaged image. The brightness that minimizes the residual in a channel is adopted as the best-fit for that channel. The error again was estimated as twice the final step size, the final difference between neighboring brightness values we tried, which is 1/16 of the best-fit brightness value.

Figure 3 shows a KLIP SDI reduction of the disk in IFS, the best-fit model disk produced by ZODIPIC, and the KLIP SDI reduction of the raw data with the best-fit model subtracted. KLIP SDI was chosen to display the before and after disk model subtraction as it has the least speckle noise, even though SDI processing was not used for the actual disk modeling. The best-fit disk model was only processed with SDI for display. With ZODIPIC, we found the best-fit model has a position angle and inclination of $P.A. = 27.0^\circ \pm 1.0$ and $i = 80.0^\circ \pm 1.0$. Our model estimated the disk radius at 46.0 ± 2.0 au and that the projected center of the disk is minimally offset from the central star, with best-fit $\Delta x, \Delta y = -1.0 \pm 0.5, 0.5 \pm 0.5$ au.

Since we did not directly probe the inner and outer disk radius with our ZODIPIC model, we must consider what the disk radius indicates further. Scattered light observations mostly probe those small grains that can strongly be affected by interaction with stellar radiation forces or wind. Pushed

onto eccentric or unbound orbits by the radiation pressure these small particles can form an extended halo outside the ring of parent planetesimals. Such halos can make difficult the accurate determination of the planetesimal belts' outer edge in scattered light observations, however we can reasonably assume that the peak of the surface brightness distribution is coincided with the planetesimal belt thereby probing its location. Though the presence of gas can alter this picture in special cases (Richert et al. 2018), sensitive observation of HD 115600 with the ALMA interferometer found no gas (Liemman-Sifry et al. 2016), therefore in the following the belt is assumed to be located at a radius of 46 au.

We performed a secondary, independent geometric analysis using the same ellipse fitting method used originally by Currie et al. 2015b on HD 115600 and described in Thalmann et al. 2011. First, we applied a median filter (FWHM, ~ 4 pixels width) to the classical ADI image of the disk to reduce the pixel-to-pixel noise. We then constructed a large grid of ellipses ($\sim 10,000$) around the best-fit disk model as determined by ZODIPIC and find a new best-fit geometry as the ellipse which contains the highest average signal within its trace. The center of the image (~ 25 au) was again masked out for this analysis to avoid contributions from the strong speckle noise.

The best-fit ellipse trace is shown superimposed over the disk in Figure 3. It has projected semi-major and minor axes of $a = 44.5 \pm 0.8, b = 8.9 \pm 0.8$ au corresponding to an inclination of $i = 78.5^\circ \pm 1.0$, with a position angle $P.A. = 27.5^\circ \pm 1.1$. The disk center is offset $\Delta x, \Delta y = 0.8 \pm 0.6, 0.0 \pm 0.6$ au. Uncertainty is again estimated as twice the step size. We also perform the same analysis on KLIP ADI and SDI images. In those cases, we achieve consistent results, and the estimated disk offset is actually smaller.

5. DISCUSSION

5.1. Disk Offset

A disk pericenter offset can be caused by gravitational perturbations from one or more exoplanets in close proximity to the disk, and thus is an indication that unseen planets may be present. Many other disks in Sco-Cen have shown structures and asymmetries, including HD 106906 (Kalas et al. 2015), HD 111520 (Draper et al. 2016), HD 110058 (Kasper et al. 2015), HIP 67497 (Bonnefoy et al. 2017), etc.

Both disk modeling methods individually indicate there may be a small (~ 1 au) projected disk offset in the x -direction, but do not agree on which direction, and are consistent with zero offset within 2σ errors. Offsets on the order of ~ 1 au are at the scale of one IFS pixel, and are therefore difficult to determine precisely. Thus, we are only able to constrain that the projected offset does not exceed ~ 1.5 au in either direction.

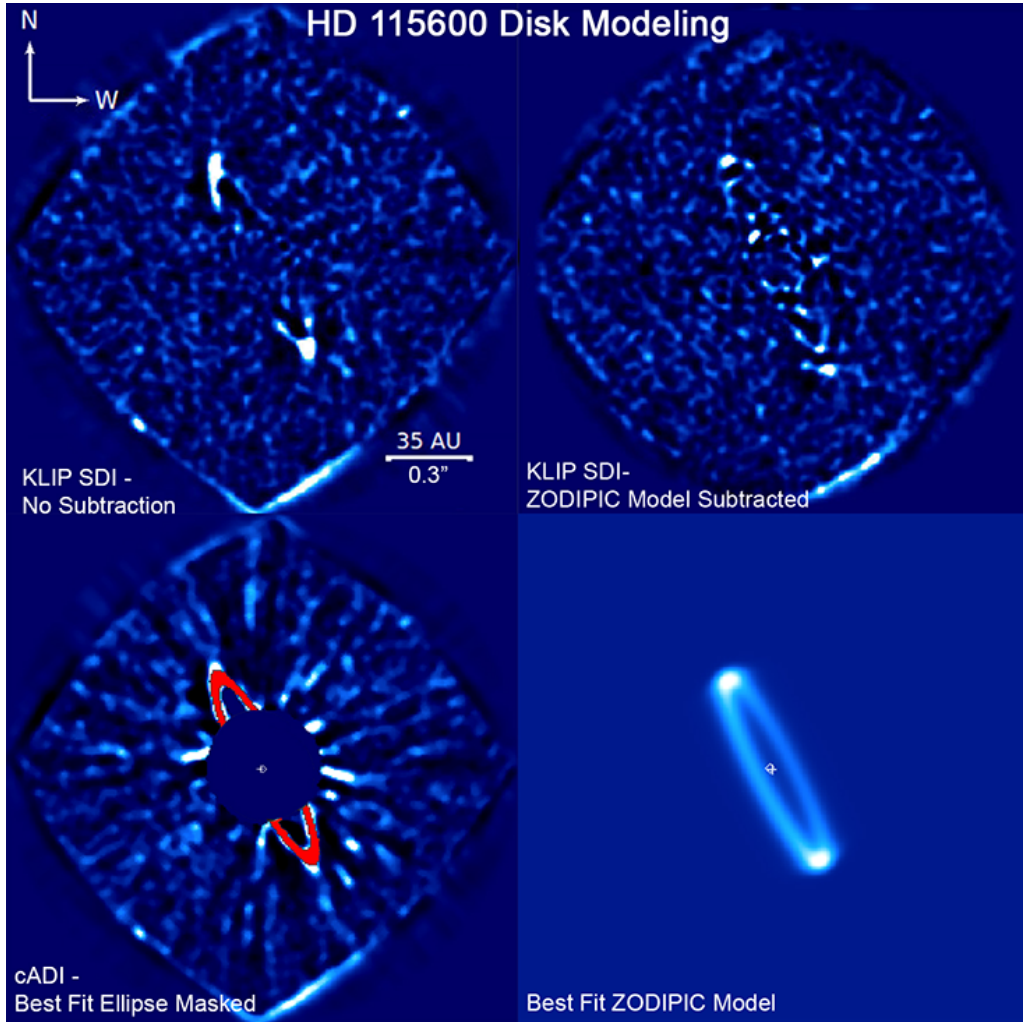


Figure 3. Disk Modeling. Top Left: Band-averaged, KLIP SDI reduction of IFS images without subtraction. Top Right: The same reduction with the best-fit disk model from ZODIPIC subtracted. Bottom Left: Best fit ellipse model in green over classical ADI reduction. Noise from the central star is masked to ~ 25 au. Bottom Right: ZODIPIC best-fit model which is used for subtraction. The star center marked by a cross. The centers of the respective disk models are marked with diamonds.

Table 2. ZODIPIC Disk Modeling

Parameter	Range Tested	Step Size	Best Fit	Uncertainty
Disk Radius (au)	45 to 49	1.0	46	± 2.0
Position Angle (deg)	23 to 29	0.5	27	± 1.0
Inclination (deg)	78 to 81	0.5	80	± 1.0
x Offset (au)	-1 to 4	0.25	-1.0	± 0.5
y Offset (au)	-1 to 4	0.25	0.5	± 0.2

Our results on the disk eccentricity imply that any unseen exoplanets are likely less massive than previously estimated. Using the projected disk offset estimated by Currie et al. (2015b), Thilliez & Maddison (2017) showed that a $7.8 M_J$ planet could be present in the system at 30 au with an eccentricity of $e = 0.2$, which could be detected by SPHERE or GPI. Due to the inclination of the system, however, there is a high probability that the planet would lie within the inner working angle of both instruments, and thus undetected. If the disk eccentricity is smaller, though, planets far less massive than $7.8 M_J$ may be able to sculpt the disk, plausibly low enough to elude detection in our data and those in Currie et al. 2015b.

5.2. Stirring of the Disk

Planetesimals must be stirred to produce smaller and smaller fragments and finally dust via their collisions (Matthews et al. 2014). This stirring could either be related to large planetesimals embedded in the belt (self-stirring, Kenyon & Bromley 2008) or a giant planet(s) located somewhere in the system (planetary stirring, Mustill & Wyatt 2009). In the following we will explore whether the self-stirring scenario is feasible in the HD 115600 system or we need a giant planet to explain the dust production. In the classical self-stirring model collisional coagulation among smaller bodies leads to the formation of Pluto-sized ($r \sim 1000$ km) planetesimals that then can ignite a collisional cascade in the belt via their dynamical perturbation (Kenyon & Bromley 2008). The larger the radial distance and the smaller the surface density of the disk, the longer is the time needed for the buildup of these large bodies. Kenyon & Bromley (2008) provided an analytical formula for this timescale: $t_{1000} = 145 x_m^{-1.15} (a/80 \text{ au})^3 (2M_\odot/M_*)^{3/2} [\text{Myr}]$. Here a is the radial distance, while the x_m parameter scales with the initial surface density, in the case of the minimum-mass solar nebula $x_m = 1$. Adopting the 15 Myr estimated age of HD 115600 as the available time for the formation of Pluto-sized bodies and a primary stellar mass of $1.5 M_\odot$ (taken from Chen 2014), we found that a disk with $x_m \sim 2.5$ is enough to explain the stirring at 46 au. Alternatively, according to turbulent concentration and gravitational clumping models (Johansen et al. 2007; Cuzzi et al. 2008) large planetesimals can form directly from the concentration of small pebbles in a protoplanetary disk. Though these models predict very rapid formation of hundred kilometer size bodies even at radii > 100 au (Carrera et al. 2017), additional time is needed to excite the neighbouring disk sufficiently (Krivov & Booth 2018). According to equation 34 from Krivov & Booth (2018) in this model the stirring of the belt at a time of 15 Myr needs an even lower initial surface density ($x_m \sim 0.3$) than in the case of the gradual buildup approach. Obviously, the initial surface density could not be arbitrarily large: ac-

ording to Mustill & Wyatt (2009), $x_m > 10$ would imply that the self-stirring scenario may not be feasible in the given system raising the suspicion that the dynamical excitation is rather related to a planet. The obtained low x_m values thus indicate that self-stirring can work in the HD 115600 systems and it is not necessary to assume the presence of a giant planet.

5.3. Analysis of the Spectral Energy Distribution

The spectral energy distribution (SED) of a stellar system can be used to determine if there are one or more circumstellar disk components based on the number of temperature peaks. If a disk has two spatially distinct components, the inner component will be warmer than the outer component and both will have unique blackbody distributions visible in the SED. Examining the SED of HD 115600, we can determine if there may be an inner disk component not visible in our data.

By modeling the SED of HD 115600, Chen (2014) proposed a two-temperature disk model with $T_{d,\text{warm}} = 499$ K and $T_{d,\text{cool}} = 109$ K to fit the observed mid- and far-infrared (far-IR) excess. Similar analyses of Ballering et al. (2013) and more recently Currie et al. (2015b), however, led to single component models at temperatures of 109 and 115 K, respectively. All of these results were based on measurements shortward of $70 \mu\text{m}$. In order to better characterize the far-IR SED of our target we examined unpublished 100 and $160 \mu\text{m}$ observations obtained with the PACS instrument onboard the Herschel Space Observatory. We used the Herschel Interactive Processing Environment (HIPE v13, Ott 2010) to process the data following the basic steps described in Moór et al. (2015). HD 115600 is detected at both wavelengths, however at $160 \mu\text{m}$ it is contaminated by surrounding extended emission therefore no photometry was derived. At $100 \mu\text{m}$ our aperture photometry yielded a flux density of 138 ± 12 mJy. The aperture radius was set to $6''$, the sky background was measured in an annulus between $40''$ and $50''$. The quoted uncertainty is a quadratic sum of the measurement and calibration (7%, Balog et al. 2014) errors. To compile the final SED, previously obtained infrared photometric and spectroscopic data taken from the literature and public databases (Wright et al. 2010; Ishihara et al. 2010; Lebouteiller et al. 2011; Chen 2014) were supplemented by our new $100 \mu\text{m}$ and a recent 1.24 mm (?) photometry of the source. To estimate the photospheric contribution at relevant wavelengths an ATLAS9 model (Castelli & Kurucz 2003) was fitted to the optical and near-IR photometric data of HD 115600 (taken from Perryman 1997; Høg et al. 2000; Cutri et al. 2003). Based on our analysis of the source's Strömgren photometry (Paunzen 2015) the influence of reddening was neglected, while for the metallicity a value of $[\text{Fe}/\text{H}] = -0.16$ was derived using the method proposed by Casagrande et al. (2011).

By fixing $[\text{Fe}/\text{H}] = -0.16$ as well as $\log g = 4.25$ (i.e. assuming the primary is a young dwarf star of slightly subsolar metallicity) a good best fit photospheric model was achieved using $T_{\text{eff}} = 6850$ K, consistent with an F2V star (Mamajek http://www.pas.rochester.edu/~emamajek/EEM_dwarf_UBVIJHK_colors_Teff.txt). Figure 4 displays the SED and the obtained photosphere model of our target.

After the subtraction of the photospheric contribution, the excess SED was fitted by 1) a single temperature modified blackbody model where the emissivity is 1 at wavelengths shorter than $100\mu\text{m}$ and varies as $(\lambda/100\mu\text{m})^\beta$ at longer wavelengths, and 2) by a two-temperature model where the single modified blackbody component was complemented with a warmer simple blackbody. We utilized a Levenberg-Marquardt algorithm (Markwardt 2009) to find the best-fitting model. In good accordance with Ballering et al. (2013) and Currie et al. (2015b) we found that the SED is adequately described by a single modified blackbody with $T_{\text{dust}} = 111 \pm 3$ K, $\beta = 0.92 \pm 0.22$, and $L_{\text{disk}}/L_{\text{bol}} = 0.002$.

5.4. Dust-rich Debris Disks around F-G-type Sco-Cen members

HD 115600 is a member of the Sco-Cen association. To put into context our results on its disk parameters in the following we make a comparison with other dust-rich debris disks in the same group. Using *Spitzer* $24\mu\text{m}$ photometric data Chen et al. (2011) inferred an excess fraction of $\sim 33\%$ for F-G-type members of the Sco-Cen association. Eleven out of the revealed disks were found to exhibit fractional luminosity higher than 10^3 , and ten from this bright disk subsample, including HD 115600, harbored dust colder than 150 K. Observations of these ten dust-rich systems with ground-based high-contrast imaging systems such as SPHERE and GPI in scattered light and with the ALMA interferometer at millimeter wavelengths resulted in spatially resolved disk images in all but one case (HD 117214). Fundamental properties of these objects, derived based on their resolved images and analysis of their SED, are summarized in Table 3.

The radii of the resolved dust belts range between 30 and 80 au. With its radius of 46 au, HD 115600 is the second smallest object after the disk of HD 114082 and resembles our Kuiper-belt the most among all the targets (see also Currie et al. 2015b). The ratio of the disk sizes derived from the spatially resolved images (R_{belt}) to radii inferred from dust temperatures assuming large grains behaving as blackbodies (R_{BB}) is higher than 1 for all cases. This is a well known signature of the presence of small dust particles that, as being inefficient emitters at long wavelengths, are hotter than blackbodies (Booth et al. 2013). Small grains should not be stable under the influence of radiation pressure, and

their presence suggests an active source of supply from grinding/aggregating planetesimals and sublimating icy bodies.

Figure 5 shows the $\Gamma = R_{\text{belt}}/R_{\text{BB}}$ ratios as a function of stellar luminosity for our targets. For comparison, debris disks resolved with the Herschel Space Observatory around stars having luminosity similar to that of our study are also displayed (data for these objects were taken from table 4 of Pawellek et al. 2014). As Figure 5 demonstrates dust-rich debris disks around F-G-type members of Sco-Cen show a great variety in terms of Γ values. On the one hand HD 106906 with its Γ value close to 1 may mostly harbor larger particles. On the other hand the belts around HD 120326 and HD 146897 are significantly larger than expected using a blackbody assumption suggesting a substantial overabundance of hot small grains. Interestingly, HD 146897 is one of those rare F-type stars where CO emission was detected (?) raising the possibility that the presence of gas may play a role in accumulation of small grains in these systems e.g. by retaining those particles that would be blown out by the radiation pressure in a gas-free environment (see e.g. Wyatt 2018). As already noted by Currie et al. (2015b), HD 115600 exhibits a moderately high Γ value of ~ 3.3 indicating the presence of copious amount of small dust particles in the disk.

6. SPECTRAL ANALYSIS

We extracted YJ-band spectra from both the processed data, and from our wavelength-dependent disk model that was previously described in Section 4. Both spectra were extracted with a similar methodology to Currie et al. (2015b), to better compare our results. We first measured the average surface brightness, that is the mean pixel value, in each wavelength channel within two 8-pixel diameter apertures centered on the disk extremities in both the IFS and disk model images. These were the same regions selected in Section 3 and by (Currie et al. 2015b) for spectra, and contain the highest signal-to-noise. We converted these raw surface brightnesses into reflectance spectra (i.e., the relative brightness of the disk compared to HD 115600) by dividing the peak value of the flux calibration PSF in each wavelength, as determined by a Gaussian fit (IDL routine GAUSS2DFIT). The spectra from both disk ansa were then averaged together to produce a combined spectrum. Unfortunately, we found that the spectrum produced from the processed IFS data suffers from significant variability due to speckle noise, and therefore only kept the combined reflectance spectrum from our model for analysis. The uncertainty in the model reflectance spectrum is determined as a combination of the measured speckle noise in each wavelength channel (using the same method from Section 3), and the brightness uncertainty in the model from the grid step size, discussed in Section 4.

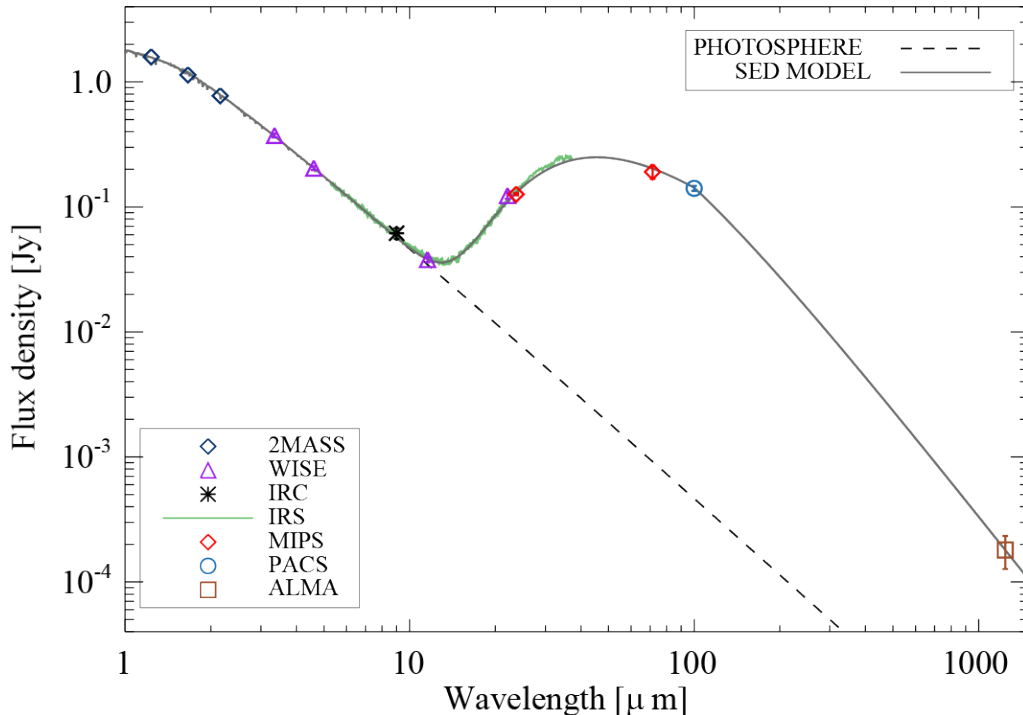


Figure 4. Spectral energy distribution of HD 115600 overplotted by the fitted modified blackbody model.

The spectrum of a debris disk depends, among other factors, on the dust composition. By combining our SPHERE YJ-band reflectance spectrum with the GPI H-band reflectance spectrum from Currie et al. (2015b), and comparing them to reflectance models, we aim to constrain the disk composition further. To avoid biases inherent in combining the data from multiple instruments into a single spectrum, we compare the SPHERE spectrum to reflectance models individually. We choose to compare the SPHERE spectrum to the same reflectance models used in Currie et al. (2015b), for water ice, amorphous carbon, and amorphous silicate dust compositions. These models are based on simple Mie scattering theory predictions from Lisse et al. (1998) and Halley-like particle size distributions (Krishna Swamy & Shah 1988; Mazets et al. 1986), rather than more realistic calculations. To convert our reflectance spectrum into normalized units, we scale the spectrum so that the spectrum’s maximum is equal to a reflectivity of one. We then scale each reflectance model to minimize χ^2 , and the lowest is the best-fit.

Our reflectance spectrum for SPHERE is shown in Figure 6, along with the aforementioned reflectance models. It shows a reddish slope, and, without considering GPI H band spectra yet, has the best agreement with amorphous carbon and silicate compositions, marginally favoring carbon. Water ice is slightly disfavored due to its blue slope, with a χ^2 values 2 times that of amorphous carbon. The uncertainty on the spectrum, however, means that none of the reflectance

models are ruled out at the 95% confidence limit, and any of the 3 compositions could be viable.

Our spectral results in the Y-J bands suggest a more complex composition than the range of those considered in Currie et al. (2015b) using the H band. The H band spectrum from GPI data marginally favors water ice composition while disfavoring amorphous carbon, and our Y-J band spectrum from SPHERE data suggests the opposite, however, both spectra could be viable with all our reflectance models. This illustrates the difficulty of obtaining precise composition determinations of debris disks, as the spectra are mostly flat and different compositions are highly degenerate. Of course, the true disk composition is likely to be a complex mix of outer solar system materials (i.e. ices, rock, and complex organics), such that a superposition of spectra may yield a better fit. Comparing the overall Y-H colors of the HD 115600 disk with those of solar system objects can provide some clues to a mixed composition (Lisse et al. 2017, Fig. 4). As solar system objects become more active, they tend to become redder in the NIR due to increasing exposure of organic material and loss of surface ices. The active Centaur 5145 Pholus, for example, has an extremely red reflectance spectrum up to about 1.5 microns, but flattens out and becomes slightly blue at longer wavelengths, similar to YJ to H bands the trends we see for the HD 115600 disk. The trend for 5145 Pholus is known to be caused by exposed reddish complex organic materials mixed with surface ice absorption (Barucci et al. 2002). Other active Centaurs display similar behavior.

Table 3. Stellar and Disk Parameters

Name	Spt.	Dist.	Lum.	Group	$L_{\text{disk}}/L_{\text{bol}}$	T_{dust}	Ref.	R_{BB}	R_{belt}	Ref.
(1)	(2)	(3)	(4)	(5)	$\times 10^{-3}$	(K)	(8)	(9)	(10)	(11)
HD 106906	F5V	103.3	6.56	LCC	1.8	53*	1	70.5	71	4
HD 111520	F5/F6V	108.9	2.58	LCC	1.5	49*	3	51.7	70	2
HD 114082	F3V	95.7	3.86	LCC	4.3	110	1	12.5	31	7
HD 115600	F2IV/V	109.6	4.84	LCC	2.0	111	4	13.8	46	8
HD 120326	F0V	113.9	4.51	UCL	2.2	114	1	12.6	62	1
HD 129590	G3V	136.0	2.98	UCL	7.7	89	1	16.9	57	6
HD 145560	F5V	120.4	3.24	UCL	3.9	53*	1	49.5	79*	5
HD 146181	F6V	125.0	2.73	UCL	3.0	71*	1	25.3	79*	5
HD 146897	F2/F3V	131.5	3.29	US	5.6	94*	2	15.9	78	3

NOTE— Column (1): Target name. Column (2): Spectral type (from SIMBAD). Column (3): Distance (from *Gaia* DR2 parallax, [Lindegren et al. 2018](#)). Column (4): Luminosity. Data were taken from *Gaia* DR2 catalogue ([Lindegren et al. 2018](#); [Andrae et al. 2018](#)) except for HD 115600 where we used our own estimate. Column (5): Group membership. LCC: Lower Centaurus Crux association; UCL: Upper Centaurus Lupus association; US: Upper Scorpius association. Column (6): Fractional luminosity of the disk. Column (7): Dust temperature. For two-temperature disks (marked by asterisks) the temperature of the colder component was quoted. Column (8): Reference for dust temperature. (1) [Ballering et al. \(2013\)](#); (2) [Chen \(2014\)](#); (3) [Draper et al. \(2016\)](#); (4) this work. Column (9): Disk radius estimated from the characteristic dust temperature assuming grains act like blackbodies ($\frac{R_{\text{BB}}}{\text{au}} = \left(\frac{L_{\text{star}}}{L_{\odot}}\right)^{0.5} \left(\frac{278\text{K}}{T_{\text{disk}}}\right)^2$). Column (10): Disk radius derived from spatially resolved scattered light or millimeter images. For scattered light data the radius of peak dust density was adopted, in the case of millimeter data (marked by asterisks) the average between the inner and outer belt radii were used. The original estimates (for references see Col. 11) were recomputed considering the new *Gaia* DR2 distances. Column (11): Reference for R_{belt} values: (1) [Bonnetfoy et al. \(2017\)](#); (2) [Draper et al. \(2016\)](#); (3) [Engler et al. \(2017\)](#); (4) [Lagrange et al. \(2016\)](#); (5) [Lieman-Sifry et al. \(2016\)](#); (6) [Matthews et al. \(2017\)](#); (7) [Wahhaj et al. \(2016\)](#); (8) this work.

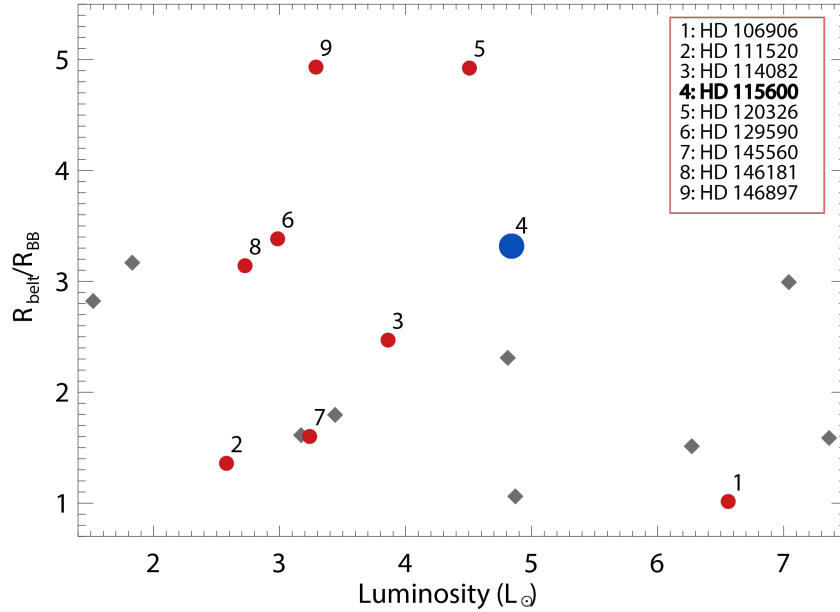


Figure 5. The ratio of the measured disk radius to its blackbody radius as a function of stellar luminosity. Dust-rich debris disks around Sco-Cen members are displayed by red circles while disks from [Pawellek et al. \(2014\)](#) are marked by gray diamonds.

By contrast, highly processed short period comets maintain a reddish color out to 4-5 microns due to their extreme activity and solar processing (Quirico et al. 2016). Interestingly enough, the approximately 100K dust in the bright ring surrounding A0.5V HR4796A at 75 AU distance matches this behavior (Lisse et al. 2017). On the other hand, pristine Kuiper Belt Objects (KBOs) at $T < 50\text{K}$ evince mostly neutral or blue spectra due to the dominance of abundant ices (CO, CH₄, N₂, H₂O) on their surfaces. We can therefore hypothesize that the HD115600 disk has a mixed composition and is composed of dust emitted from large semi-active planetesimals.

7. PLANET DETECTION LIMITS

While no wide-orbit giant planet is obviously detected in our data, the lack of detection places useful constraints on the presence of planets external to the disk (projected radii > 50 au). To analyze our detection threshold we injected false-positive point sources at 4×10^{-5} contrast into the raw data prior to processing. We then measured the brightness of the recovered sources compared to the originally injected PSF, and utilized the average recovered contrast to estimate the throughput correction appropriate for the data processing. We find that the throughput correction is essentially uniform with radius exterior to the disk, and thus we adopt a constant correction throughout the image. To compute a detection threshold for each radius, we integrated the flux in non-overlapping apertures of radius equivalent to the beam FWHM while accounting for small sample statistics (Mawet et al. 2014). We multiplied the standard deviation of these measurements at a particular radius by the throughput correction factor and scaled this by a factor of five to arrive at the reported 5σ contrast limit shown in Figure 7. This analysis suggests that we would have confidently detected a point source of 5×10^{-6} ($H < 20.6$) between the outer edge of the disk and 100 au, or a source of 2×10^{-6} ($H < 21.6$) between 100-200 au. Compared to hot(cold)-start evolutionary models (Baraffe et al. 2003; Marley et al. 2007; Morasini 2013) which give theoretical planet luminosities at the system’s age, these brightness measurements correspond to mass limits of 3-4 (7-12) and 2-3 (5-7) M_J , respectively, depending on the core mass.

8. SUMMARY

We present new extreme adaptive optics (VLT/SPHERE) imaging of the debris disk surrounding the young star HD 115600. Our dataset improves characterization of the surrounding debris disk and upper limits on possible exoplanets embedded in the disk. We model the debris disk to investigate structure that could indicate unseen exoplanet(s), as suggested by Currie et al. (2015b) and Thilliez & Madisson (2017). We determine disk geometry by two methods, using the code ZODIPIC (Kuchner 2012) to inject and subtract a grid of disk models into the raw data, and by a ‘maximum merit’ ellipse fitting method on the ADI images, as described in Thalmann et al. (2011). The key findings of our study are as follows:

1) We confidently detect the disk ($\text{SNR} \sim 20$) at separations between $0.35''$ and $0.48''$ and at wavelength between $1.0 \mu\text{m}$ and $1.6 \mu\text{m}$ and present near diffraction-limited images at these wavelengths.

2) Using ZODIPIC, we determine a best-fit disk model with central radius $a_0 = 46 \pm 2\text{au}$, inclination $i = 80^\circ \pm 1$, position angle of $27^\circ \pm 1$, and offsets $\Delta\alpha, \Delta\delta = -1.0 \pm 0.5, 0.5 \pm 0.5$ au. By ellipse fitting, we determine a best-fit disk model with projected semimajor axis $a = 44.5 \pm 0.8$ au, inclination $i = 78.5^\circ \pm 1.0$, position angle of $27.5^\circ \pm 1.1$, and offsets of $\Delta\alpha, \Delta\delta = 0.8 \pm 0.6, 0.0 \pm 0.6$ au.

The disk offset is smaller than previous estimates derived from modeling with the H-G scattering function. As a result, planets responsible for sculpting the debris disk could be significantly lower in mass than previously estimated.

3) Using SPHERE IFS, we produce a YJ-band reflectance spectrum for the disk, which is reddish, and marginally supports an amorphous carbon composition, although other compositions cannot be decisively ruled out. Considering the flat to slightly blue H band reflectance previously seen with GPI and a survey of our solar system’s small body reflectance spectra, the combined results are consistent with a mixed organic and water ice dust composition typical of our solar system’s active Centaurs interacting with the giant planets and the Sun.

4) We constrain a mass sensitivity limit of 3-4(7-12) M_J with 100 au of the star, and 2-3(5-7) M_J within 100-200 au by combining contrast limits from fake planet injections with hot(cold)-start model predictions.

APPENDIX

A. PROPERTIES OF DETECTED POINT-SOURCES

To investigate the nature of the sources in the SPHERE and GPI images, we list the astrometry in tables 4 and 5, and the astrometric difference of commonly detected sources in table 6. Note that source 1 is a likely disk feature as it falls within the region of the scattered light ring. Sources 2-4 exhibit motions in a consistent direction with one another, and consistent with the reflex motion of the proper motion of HD 115600, and thus we classify these sources as background stars.

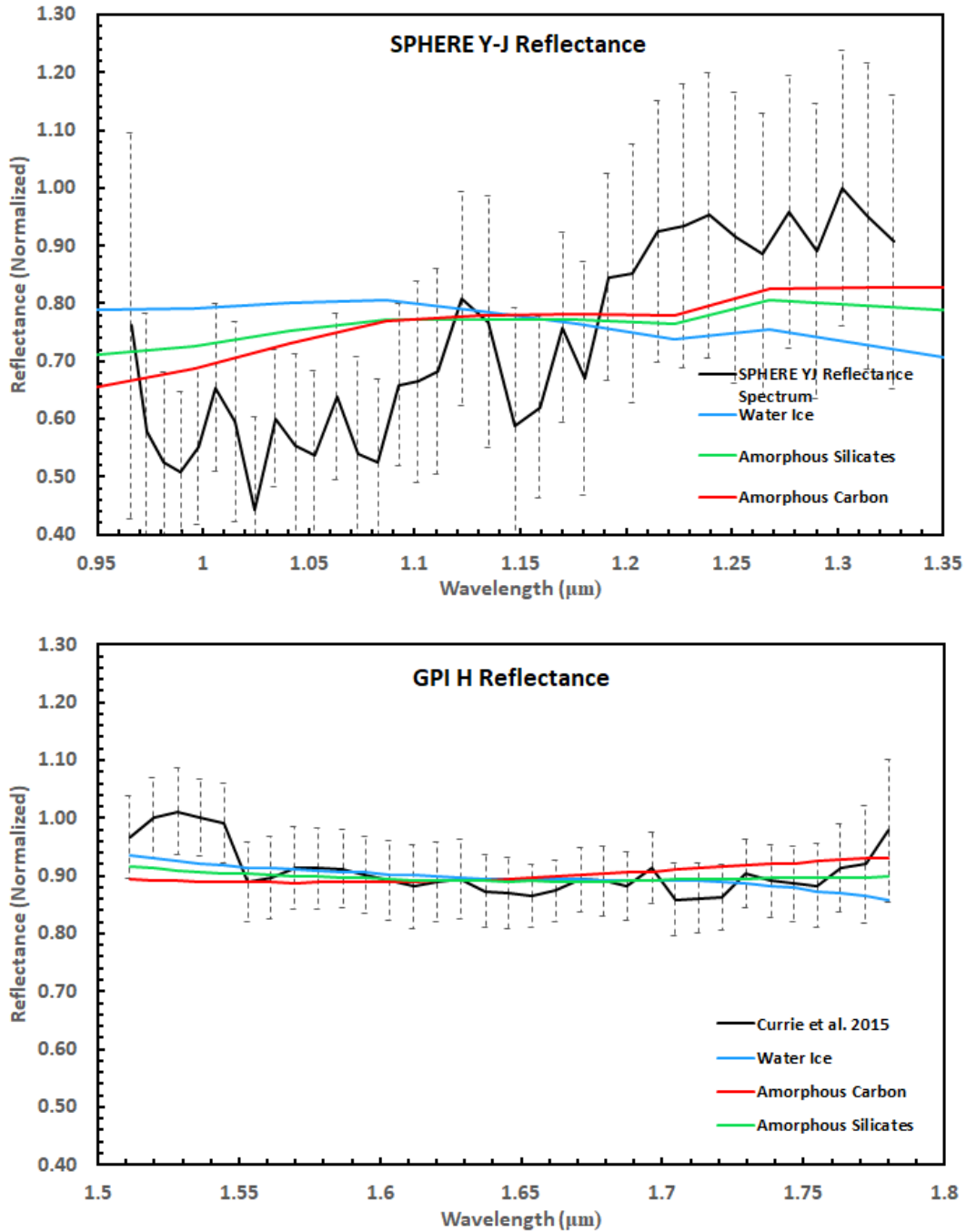


Figure 6. HD 115600 reflectance spectra. Reflectance spectra (black) from SPHERE YJ-band (top) and GPI H-band (bottom) compared to Mie theory predictions for water ice, amorphous carbon, and amorphous silicates (Currie et al. 2015b). Each reflectance model is shown scaled to best-fit the spectra.

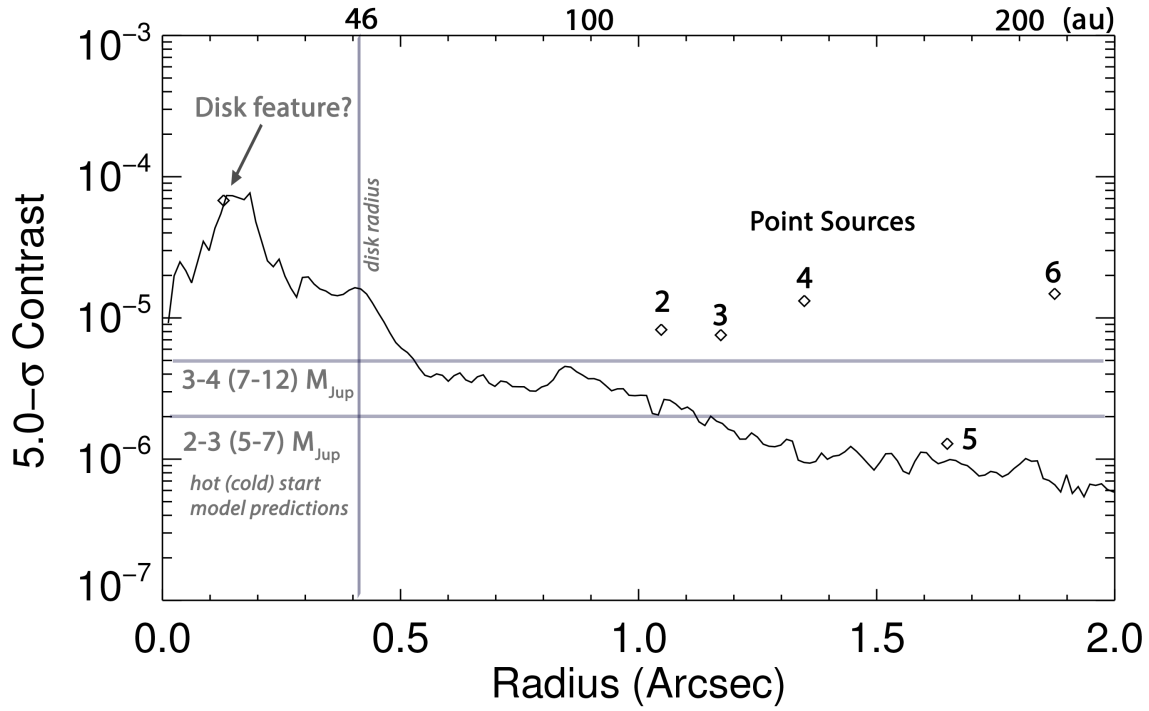


Figure 7. Radial sensitivity for the KLIP reduction of IRDIS H23 Data. The disk is clearly present and limits sensitivity around 0.2 arcseconds. Mass sensitivity limits from hot and cold start model predictions (Baraffe et al. 2003; Marley et al. 2007; Mordasini 2013) are shown as horizontal lines. Within the IFS field-of-view (~ 1 arcsecond), we achieve a sensitivity of $\sim 3-4(7-12)M_{Jup}$ for hot (cold) start models. Limits may be slightly higher for particularly dusty, cloudy planets that are slightly underluminous in H band (e.g. Currie et al. 2011, 2018; De Rosa et al. 2016). The contrast of several point-sources within the IRDIS field-of-view are numbered.

Table 4. Properties of Point-Sources detected around HD 115600 in the IRDIS Field

Source	SNR	Contrast	ρ (")	θ (deg)
1	5.81	6.78×10^{-5}	0.1284	53.69
2	14.69	8.25×10^{-6}	1.0476	211.60
3	22.14	7.56×10^{-6}	1.1727	63.03
4	47.91	1.32×10^{-5}	1.3481	202.95
5	6.81	1.29×10^{-6}	1.6482	144.53
6	76.50	1.48×10^{-5}	1.8739	222.25
7	23.77	2.67×10^{-6}	2.1634	272.49
8	5.11	6.04×10^{-7}	2.4740	259.48
9	9.51	1.04×10^{-6}	2.6082	290.10
10	11.66	1.26×10^{-6}	2.6159	103.44
11	53.06	6.48×10^{-6}	2.8354	306.45
12	420.11	5.05×10^{-5}	2.8929	3.56
13	290.13	3.51×10^{-5}	2.9851	217.98
14	36.92	3.30×10^{-6}	3.2857	69.59
15	9.65	8.88×10^{-7}	3.3603	322.31
16	17199.3	0.00154	3.3732	63.39
17	17.74	2.14×10^{-6}	3.4622	209.25
18	110.93	2.65×10^{-5}	3.5305	339.53
19	221.18	4.08×10^{-5}	3.5837	190.02
20	7.70	1.13×10^{-6}	3.6186	328.37
21	22.01	2.25×10^{-6}	3.7714	104.46
22	7.54	7.95×10^{-7}	3.7861	245.12
23	94.40	9.20×10^{-6}	3.9049	210.63
24	6.02	7.07×10^{-7}	3.9917	284.77
25	11.50	1.32×10^{-6}	3.9924	301.10
26	111.28	1.47×10^{-5}	4.0119	134.29
27	68.16	6.44×10^{-6}	4.0512	122.57
28	6.21	6.32×10^{-7}	4.1346	208.78
29	89.68	8.20×10^{-6}	4.2913	155.16
30	56.24	5.10×10^{-6}	4.6783	316.74
31	190.46	2.12×10^{-5}	4.7166	38.88
32	130.87	1.18×10^{-5}	4.9489	45.61
33	3203.20	0.0002726	5.0191	88.65
34	7.90	6.53×10^{-7}	5.0434	353.76

NOTE—Column(1): Sources as numbered in Figure 2 and Figure 7. Column(2): Detection significance. Column(3): Contrast to HD 115600. Column(4): Separation in arc-seconds. Column(5): Position angle in degrees.

Table 5. Properties of Point-Sources detected around HD 115600 in the GPI Field

Source	SNR	ρ (")	θ (deg)
2	8.070	1.0854	213.18
3	8.15	1.1488	62.94
4	8.99	1.3737	204.12

Table 6. Astrometric Motion of Commonly Detected Sources (Relative to HD 115600 over 2015.42-2014.31)

Source	Δ RA (mas)	Δ Dec (mas)
2	45.1	16.2
3	22.1	9.3
4	35.6	12.4
Mean	34.2	12.6
StdDev	11.5	3.4
HD 115600	PM RA	PM Dec
GAIA DR2	-32.63 ± 0.05 mas/yr	-18.32 ± 0.05 mas/yr

Software: IDL

REFERENCES

- Ahmic, M., Croll, B., & Artymowicz, P. 2009, *ApJ*, 705, 529
- Andrae, R., Fousneau, M., Creevey, O., et al. 2018, *A&A*, 616, A8
- Apai, D., Schneider, G., Grady, C. A., et al. 2015, *ApJ*, 800, 136
- Apai, D., Kasper, M., Skemer, A., et al. 2016, *ApJ*, 820, 40
- Bailey, V., Meshkat, T., Reiter, M., et al. 2014, *ApJL*, 780, L4
- Bailey, V. P., Poyneer, L. A., Macintosh, B. A., et al. 2016, in *Proc. SPIE, Vol. 9909, Adaptive Optics Systems V*, 99090V
- Ballering, N. P., Rieke, G. H., Su, K. Y. L., & Montiel, E. 2013, *ApJ*, 775, 55
- Balog, Z., Müller, T., Nielbock, M., et al. 2014, *Experimental Astronomy*, 37, 129
- Baraffe, I., Chabrier, G., Barman, T. S., Allard, F., & Hauschildt, P. H. 2003, *A&A*, 402, 701
- Barucci, M. A., Cruikshank, D. P., Mottola, S., & Lazzarin, M. 2002, *Physical Properties of Trojan and Centaur Asteroids*, ed. W. F. Bottke, Jr., A. Cellino, P. Paolicchi, & R. P. Binzel, 273
- Beuzit, J.-L., Feldt, M., Dohlen, K., et al. 2008, in *Proc. SPIE, Vol. 7014, Ground-based and Airborne Instrumentation for Astronomy II*, 701418
- Bonnefoy, M., Milli, J., Ménard, F., et al. 2017, *A&A*, 597, L7
- Booth, M., Kennedy, G., Sibthorpe, B., et al. 2013in (Cambridge University Press), 330
- Bottom, M., Ruane, G., & Mawet, D. 2017, *Research Notes of the American Astronomical Society*, 1, 30
- Carpenter, J. M., Bouwman, J., Mamajek, E. E., et al. 2009, *ApJS*, 181, 197
- Carrera, D., Gorti, U., Johansen, A., & Davies, M. B. 2017, *The Astrophysical Journal*, 839, 16
- Casagrande, L., Schönrich, R., Asplund, M., et al. 2011, *A&A*, 530, A138
- Castelli, F., & Kurucz, R. L. 2003, in *IAU Symposium, Vol. 210, Modelling of Stellar Atmospheres*, ed. N. Piskunov, W. W. Weiss, & D. F. Gray, A20
- Chauvin, G., Desidera, S., Lagrange, A.-M., et al. 2017, *A&A*, 605, L9
- Chen, C. 2014, in *Habitable Worlds Across Time and Space, proceedings of a conference held April 28-May 1 2014 at the Space Telescope Science Institute*, P8

- Chen, C. H., Mamajek, E. E., Bitner, M. A., et al. 2011, *ApJ*, **738**, 122
- Claudi, R. U., Turatto, M., Gratton, R. G., et al. 2008, in *Proc. SPIE, Vol. 7014, Ground-based and Airborne Instrumentation for Astronomy II*, 70143E
- Currie, T., Cloutier, R., Brittain, S., et al. 2015a, *ApJL*, **814**, L27
- Currie, T., Lisse, C. M., Kuchner, M., et al. 2015b, *ApJL*, **807**, L7
- Currie, T., Burrows, A., Itoh, Y., et al. 2011, *ApJ*, **729**, 128
- Currie, T., Guyon, O., Tamura, M., et al. 2017, *ApJ*, **836**, L15
- Currie, T., Brandt, T. D., Uyama, T., et al. 2018, ArXiv e-prints, [arXiv:1810.09457 \[astro-ph.EP\]](https://arxiv.org/abs/1810.09457)
- Cutri, R. M., Skrutskie, M. F., van Dyk, S., et al. 2003, *VizieR Online Data Catalog*, 2246
- Cuzzi, J. N., Hogan, R. C., & Shariff, K. 2008, *ApJ*, **687**, 1432
- De Rosa, R. J., Rameau, J., Patience, J., et al. 2016, *ApJ*, **824**, L21
- Dohlen, K., Langlois, M., Saisse, M., et al. 2008, in *Proc. SPIE, Vol. 7014, Ground-based and Airborne Instrumentation for Astronomy II*, 70143L
- Draper, Z. H., Duchêne, G., Millar-Blanchaer, M. A., et al. 2016, *ApJ*, **826**, 147
- Engler, N., Schmid, H. M., Thalmann, C., et al. 2017, *A&A*, **607**, A90
- Fusco, T., Rousset, G., Sauvage, J.-F., et al. 2006, *Optics Express*, **14**, 7515
- Gaia Collaboration, Brown, A. G. A., Vallenari, A., et al. 2018, *A&A*, **616**, A1
- Gáspár, A., Psaltis, D., Rieke, G. H., & Özel, F. 2012, *ApJ*, **754**, 74
- Goebel, S., Currie, T., Guyon, O., et al. 2018, *AJ* submitted
- Graham, J. R., Kalas, P. G., & Matthews, B. C. 2007, *ApJ*, **654**, 595
- Hanson, J. R., & Apai, D. 2015, in *American Astronomical Society Meeting Abstracts, Vol. 225, American Astronomical Society Meeting Abstracts #225*, 258.13
- Høg, E., Fabricius, C., Makarov, V. V., et al. 2000, *A&A*, **357**, 367
- Hong, S. S. 1985, *A&A*, **146**, 67
- Hughes, A. M., Duchêne, G., & Matthews, B. C. 2018, *ARA&A*, **56**,
- Ishihara, D., Onaka, T., Kataza, H., et al. 2010, *A&A*, **514**, A1
- Jang-Condell, H., Chen, C. H., Mittal, T., et al. 2015, *ApJ*, **808**, 167
- Johansen, A., Oishi, J. S., Mac Low, M.-M., et al. 2007, *Nature*, **448**, 1022
- Kalas, P. G., Rajan, A., Wang, J. J., et al. 2015, *ApJ*, **814**, 32
- Kasper, M., Apai, D., Wagner, K., & Robberto, M. 2015, *ApJL*, **812**, L33
- Kelsall, T., Weiland, J. L., Franz, B. A., et al. 1998, *ApJ*, **508**, 44
- Kenyon, S. J., & Bromley, B. C. 2008, *ApJS*, **179**, 451
- Keppler, M., Benisty, M., Müller, A., et al. 2018, ArXiv e-prints, [arXiv:1806.11568 \[astro-ph.EP\]](https://arxiv.org/abs/1806.11568)
- Krishna Swamy, K. S., & Shah, G. A. 1988, *MNRAS*, **233**, 573
- Krivov, A. V., & Booth, M. 2018, *Monthly Notices of the Royal Astronomical Society*, **479**, 3300
- Kuchner, M. 2012, ZODIPIC: Zodiacal Cloud Image Synthesis, *Astrophysics Source Code Library*, [ascl:1202.002](https://www.astro.phys.umd.edu/ascl/code/1202.002)
- Lagrange, A.-M., Langlois, M., Gratton, R., et al. 2016, *A&A*, **586**, L8
- Langlois, M., Vigan, A., Moutou, C., et al. 2013, in *Proceedings of the Third AO4ELT Conference*, ed. S. Esposito & L. Fini, 63
- Lebouteiller, V., Barry, D. J., Spoon, H. W. W., et al. 2011, *ApJS*, **196**, 8
- Lieman-Sifry, J., Hughes, A. M., Carpenter, J. M., et al. 2016, *The Astrophysical Journal*, **828**, 25
- Lindegren, L., Hernández, J., Bombrun, A., et al. 2018, *A&A*, **616**, A2
- Lisse, C. M., A'Hearn, M. F., Hauser, M. G., et al. 1998, *ApJ*, **496**, 971
- Lisse, C. M., Sitko, M. L., Marengo, M., et al. 2017, *AJ*, **154**, 182
- Markwardt, C. B. 2009, in *Astronomical Society of the Pacific Conference Series, Vol. 411, Astronomical Data Analysis Software and Systems XVIII*, ed. D. A. Bohlender, D. Durand, & P. Dowler, 251
- Marley, M. S., Fortney, J. J., Hubickyj, O., Bodenheimer, P., & Lissauer, J. J. 2007, *ApJ*, **655**, 541
- Marois, C., Lafrenière, D., Doyon, R., Macintosh, B., & Nadeau, D. 2006, *ApJ*, **641**, 556
- Matthews, B. C., Krivov, A. V., Wyatt, M. C., Bryden, G., & Eiroa, C. 2014, *Protostars and Planets VI*, 521
- Matthews, E., Hinkley, S., Vigan, A., et al. 2017, *ApJ*, **843**, L12
- Mawet, D., Milli, J., Wahhaj, Z., et al. 2014, *ApJ*, **792**, 97
- Mazets, E. P., Aptekar, R. L., Golenetskii, S. V., et al. 1986, *Nature*, **321**, 276
- Mesa, D., Gratton, R., Zurlo, A., et al. 2015, *A&A*, **576**, 121
- Meshkat, T., Mawet, D., Bryan, M. L., et al. 2017, *AJ*, **154**, 245
- Milli, J., Vigan, A., Mouillet, D., et al. 2017, *A&A*, **599**, A108
- Moór, A., Kóspál, Á., Ábrahám, P., et al. 2015, *MNRAS*, **447**, 577
- Mordasini, C. 2013, *A&A*, **558**, A113
- Mustill, A. J., & Wyatt, M. C. 2009, *MNRAS*, **399**, 1403
- Ott, S. 2010, in *Astronomical Society of the Pacific Conference Series, Vol. 434, Astronomical Data Analysis Software and Systems XIX*, ed. Y. Mizumoto, K.-I. Morita, & M. Ohishi, 139
- Paunzen, E. 2015, *A&A*, **580**, A23
- Pavlov, A., Möller-Nilsson, O., Feldt, M., et al. 2008, in *Advanced Software and Control for Astronomy II (SPIE)*
- Pawellek, N., Krivov, A. V., Marshall, J. P., et al. 2014, *ApJ*, **792**, 65
- Pecaut, M. J., & Mamajek, E. E. 2016, *MNRAS*, **461**, 794
- Pecaut, M. J., Mamajek, E. E., & Bubar, E. J. 2012, *ApJ*, **746**, 154
- Perryman, M. A. C. 1997, in *ESA Special Publication, Vol. 402, Hipparcos - Venice '97*, ed. R. M. Bonnet, E. Høg, P. L. Bernacca, L. Emiliani, A. Blaauw, C. Turon, J. Kovalevsky, L. Lindegren, H. Hassan, M. Bouffard, B. Strim, D. Heger, M. A. C. Perryman, & L. Woltjer, 1

- Quanz, S. P., Amara, A., Meyer, M. R., et al. 2013, *ApJL*, 766, L1
- Quirico, E., Moroz, L. V., Schmitt, B., et al. 2016, *Icarus*, 272, 32
- Racine, R., Walker, G. A. H., Nadeau, D., Doyon, R., & Marois, C. 1999, *Publications of the Astronomical Society of the Pacific*, 111, 587
- Rameau, J., Chauvin, G., Lagrange, A.-M., et al. 2013, *ApJL*, 772, L15
- Richert, A. J. W., Lyra, W., & Kuchner, M. J. 2018, *ApJ*, 856, 41
- Soumer, R., Pueyo, L., & Larkin, J. 2012, *ApJ*, 755, L28
- Su, K. Y. L., Rieke, G. H., Malhotra, R., et al. 2013, *ApJ*, 763, 118
- Thalmann, C., Janson, M., Buenzli, E., et al. 2011, *ApJ*, 743, L6
- Thalmann, C., Janson, M., Buenzli, E., et al. 2013, *ApJL*, 763, L29
- Thilliez, E., & Maddison, S. T. 2017, *MNRAS*, 464, 1434
- Vigan, A., Gry, C., Salter, G., et al. 2015, *MNRAS*, 454, 129
- Vigan, A., Moutou, C., Langlois, M., et al. 2010, *MNRAS*, 407, 71
- Wahhaj, Z., Milli, J., Kennedy, G., et al. 2016, *A&A*, 596, L4
- Wright, E. L., Eisenhardt, P. R. M., Mainzer, A. K., et al. 2010, *AJ*, 140, 1868
- Wyatt, M. C. 2008, *ARA&A*, 46, 339
- Wyatt, M. C. 2018, ArXiv e-prints, [arXiv:1804.08636](https://arxiv.org/abs/1804.08636) [astro-ph.EP]